Journal of Geophysical Research: Solid Earth

Supporting Information for

The 2019–2020 Khalili (Iran) earthquake sequence — anthropogenic seismicity in the Zagros Simply Folded Belt?

Mohammdreza Jamalreyhani[1,2], Léa Pousse-Beltran[3,4], Pınar Büyükakpınar[5], Simone Cesca[2], Edwin Nissen[3], Abdolreza Ghods[6], José Ángel López-Comino[7,8,9], Mehdi Rezapour[1], Mahdi Najafi[6]

[1]Institute of Geophysics, University of Tehran, Iran.

[2]GFZ German research center for Geosciences, Potsdam, Germany.

[3]School of Earth and Ocean Sciences, University of Victoria, Victoria, British Columbia, Canada

[4]Univ. Grenoble Alpes, Univ. Savoie Mont Blanc, CNRS, IRD, UGE, ISTerre, 38000 Grenoble, France

[5]Kandilli Observatory and Earthquake Research Institute, Boğaziçi University, İstanbul, Turkey.

[6]Department of Earth Sciences, Institute for Advanced Studies in Basic Sciences, Zanjan, Iran.

[7]Instituto Andaluz de Geofísica, Universidad de Granada, Granada, Spain.

[8]Departamento de Física Teórica y del Cosmos, Universidad de Granada, Granada, Spain.

[9]Institute of Geosciences, University of Potsdam, Potsdam-Golm, Germany.

Corresponding author: Mohammadreza Jamalreyhani (m.jamalreyhani@gmail.com)

Contents of this file

Table S3: Information of relocated 115 events of the 2019–2020 Khalili seismic sequence ($M_n \geq 3.0$) using multiple-event epicentral relocation technique.

Reference.

Text S1: Details of InSAR inversion of the June 9, 2020 M_w 5.7 Khalili mainshock

We first downsampled the unwrapped line-of-sight displacements, using a Quadtree algorithm to densify data in areas of steep phase gradient around the earthquake (Jonsson et al. 2002). Using the expressions of Okada (1985), we then solved for the minimum misfit strike, dip, rake, surface projection coordinates, length, and top and bottom depths of a rectangular fault plane with uniform 0.5 m slip buried in a half-space with elastic Lamé parameters $\lambda = \mu = 2.5 \times 10^{10}$ Pa, to represent the sedimentary cover (e.g. Nissen et al., 2010, Elliot et al. 2015) In our inversion, each ascending-track interferogram (A130 and A28) was weighted half of the single descending-track interferogram (D64), and we simultaneously solved for ambiguities in their zero displacement levels and residual orbital ramps. The inversion was performed using a nonlinear downhill Powell's algorithm, with multiple Monte Carlo restarts used in order to avoid local minima (Wright et al. 1999). Having established the fault geometry in this way, we then extend the model fault plane along strike and up and down dip, subdivide it into 2 × 2 km patches, and solve for the slip and rake distribution (Funning et al. 2005).

As is commonly the case for buried reverse faulting earthquakes, the dip direction of the causative fault is unclear from the InSAR deformation alone. We therefore explored both SSW- and NNE-dipping model faults (Tables S1–S2), and chose the best model on the basis of which was most consistent with independent seismological results (hypocenter locations and focal mechanisms).

NNE-dipping model fault geometry

In this geometry, inverting the unwrapped interferograms for uniform slip on a single model fault, we obtained a fault with strike 286°, a shallow dip angle of 19°, and a rake of 91° (Table S1 and Figure S11). Solving for distributed slip reproduces the observed deformation well (RMS 7.1 mm), (Figure S12). This InSAR distributed slip model has moment magnitude M_w 5.9.

SSW-dipping model fault geometry

In this geometry, inverting for uniform slip on a single model fault yielded strike 106°, dip 66°, and rake 83° (Table S2 and Figure S13)**.** We used this geometry to produce a distributed slip model (Figure S14), which fits the observed deformation with a RMS of 7.4 mm. An additional distributed slip inversion with variable rake only slightly reduced residual displacements to 7.2 mm, so we prefer the simpler model with distributed slip but uniform rake.

This model left residual fringes around the eastern tip of the fault, motivating us to explore another uniform inversion with two faults (Table S2 and Figure S15). For a stable inversion we needed to reduce the number of free parameters, and we thus fixed the center of the faults using the shape and positions of the observed fringes. This model geometry was then used to solve for distributed slip. The resulting two model faults fit the observations better (RMS 6.5 mm) than a single fault can, and the residual fringes are much reduced. A variable rake model improves the fit only slightly (RMS 6.4 mm), and so we prefer the simpler model, with distributed slip but uniform rake.

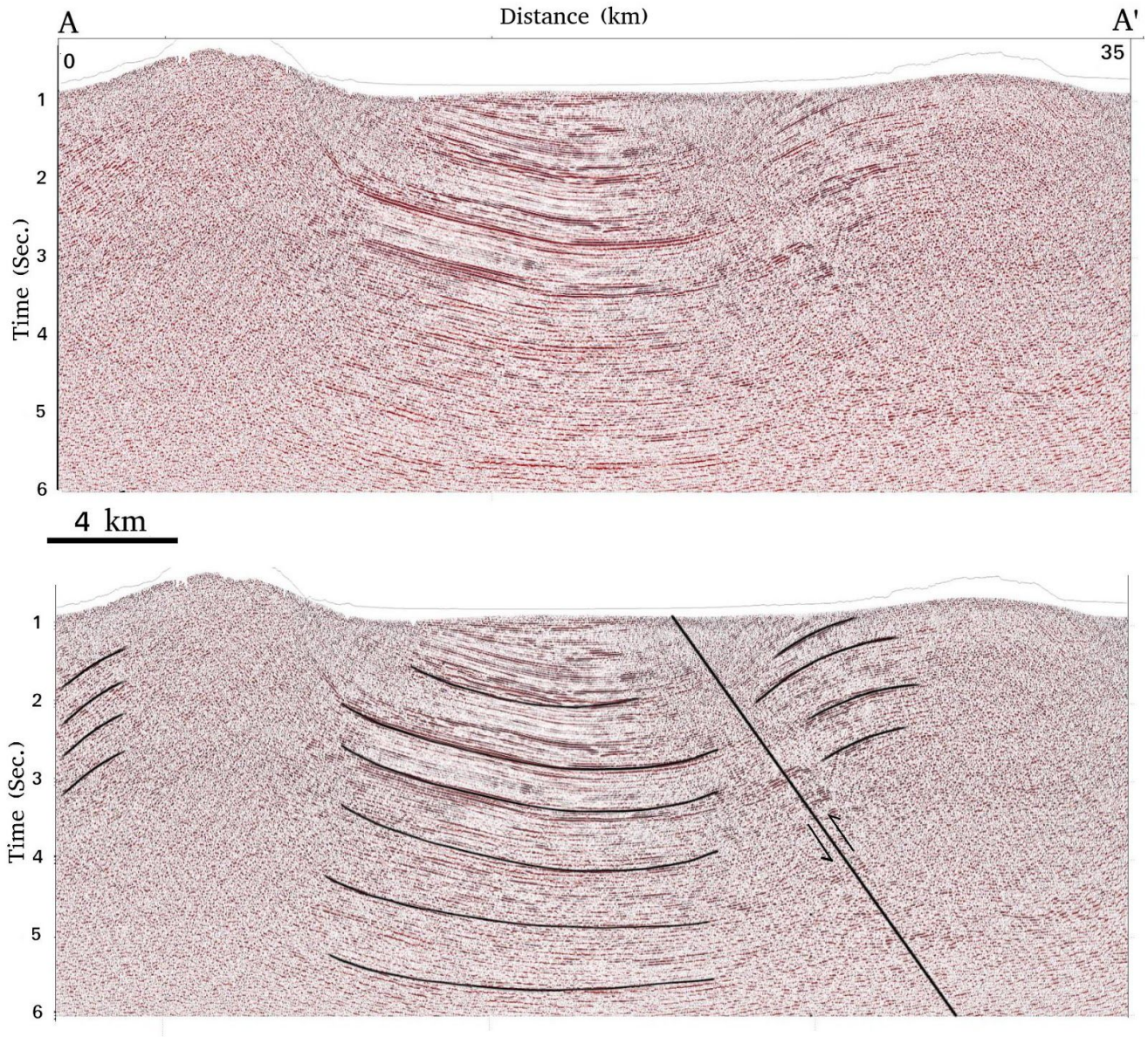

Figure S1. Seismic reflection profile across the central Varavi anticline and western Shanul anticline (profile A–A' in Figure 2). The upper panel is uninterpreted, and the lower panel interpreted with curved lines indicating prominent reflectors and the straight line indicating the approximate location of a N-dipping reverse fault. The y-axis is two way travel time.

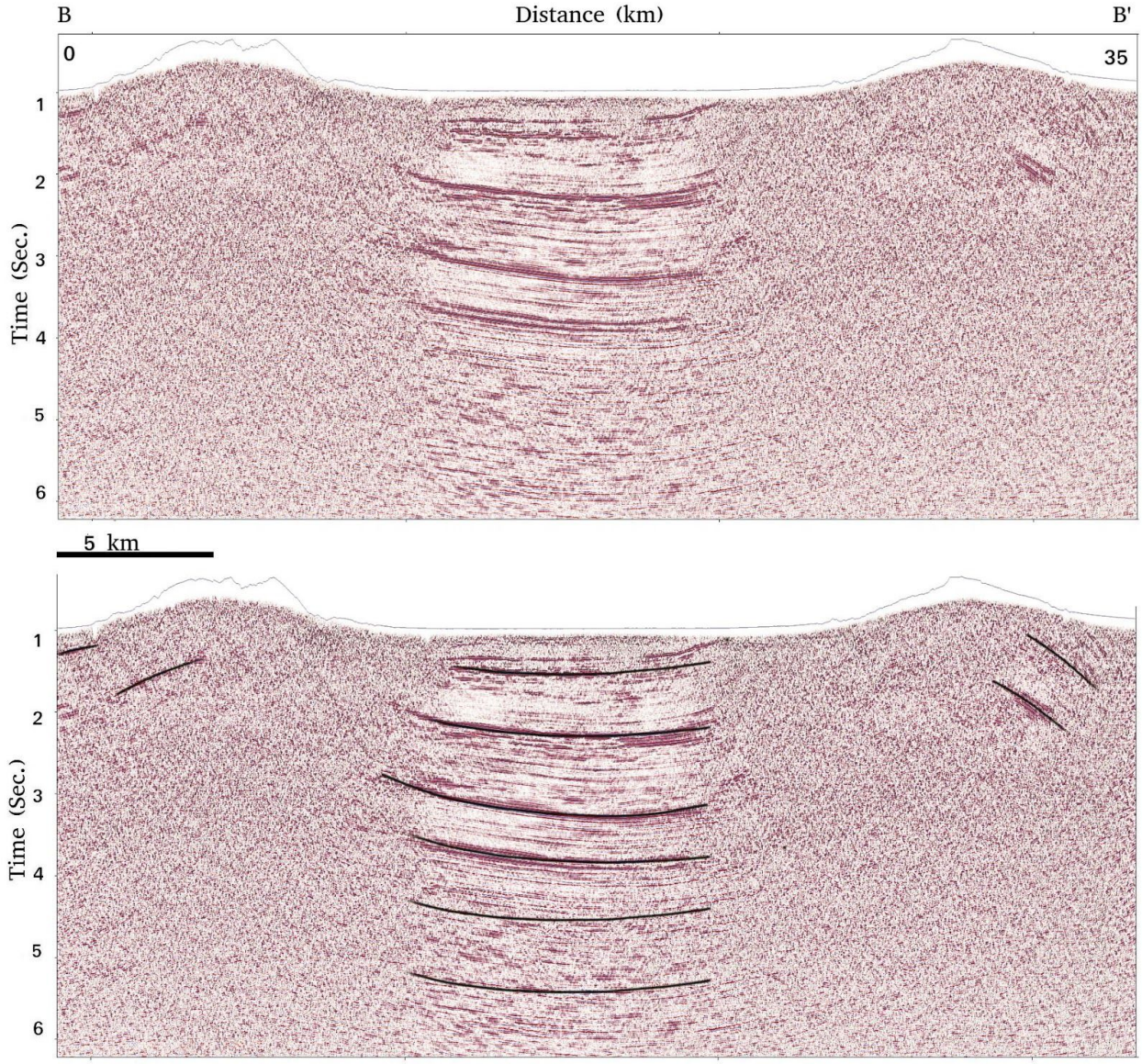

Figure S2. Seismic reflection profile across the eastern Varavi anticline and eastern Shanul anticline (profile B–B' in Figure 2). The upper panel is uninterpreted, and the lower panel interpreted with curved lines indicating prominent reflectors. The y-axis is two way travel time.

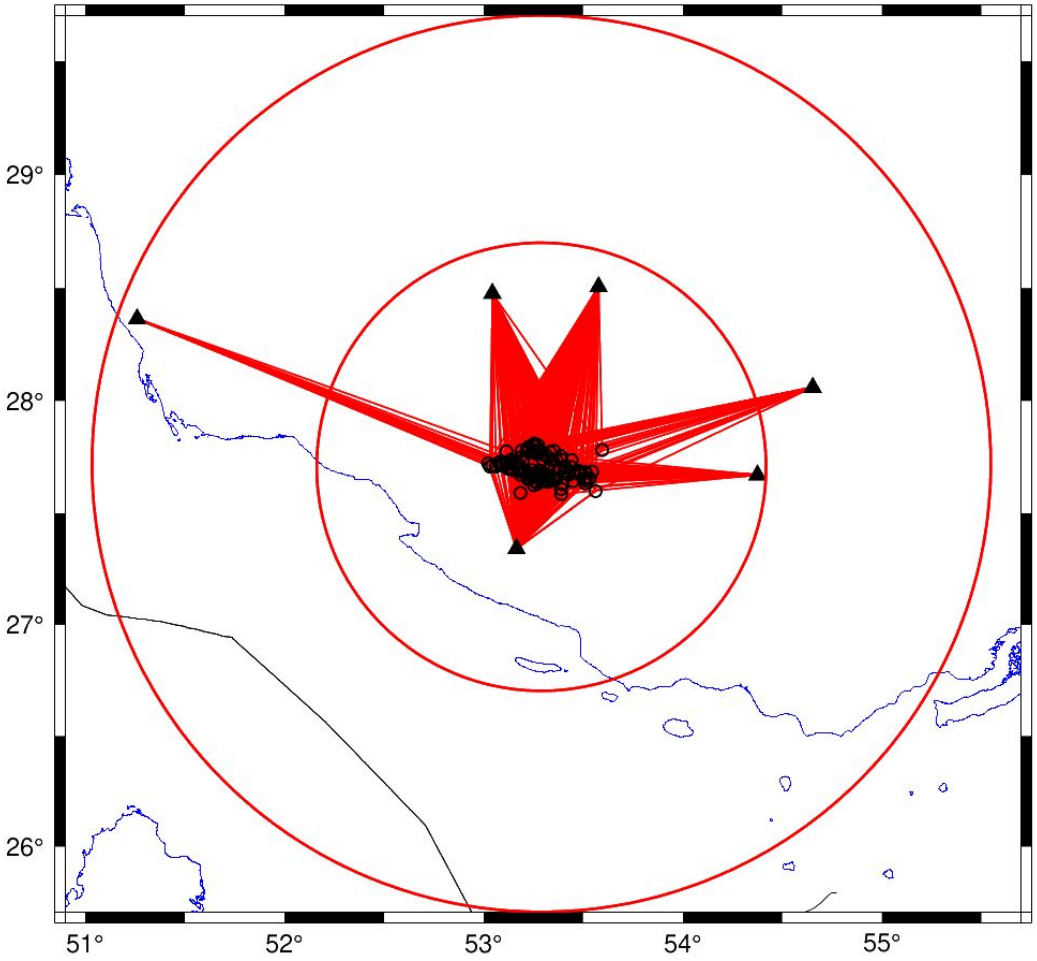

Figure S3. IRSC station distribution (black triangles) and ray paths (red straight lines) used to relocate the 2019-2020 Khalili seismic sequence (black open circles). Large red circles show radii of 100 km and 200 km from the cluster hypocentroid. These stations were also used for moment tensor inversion.

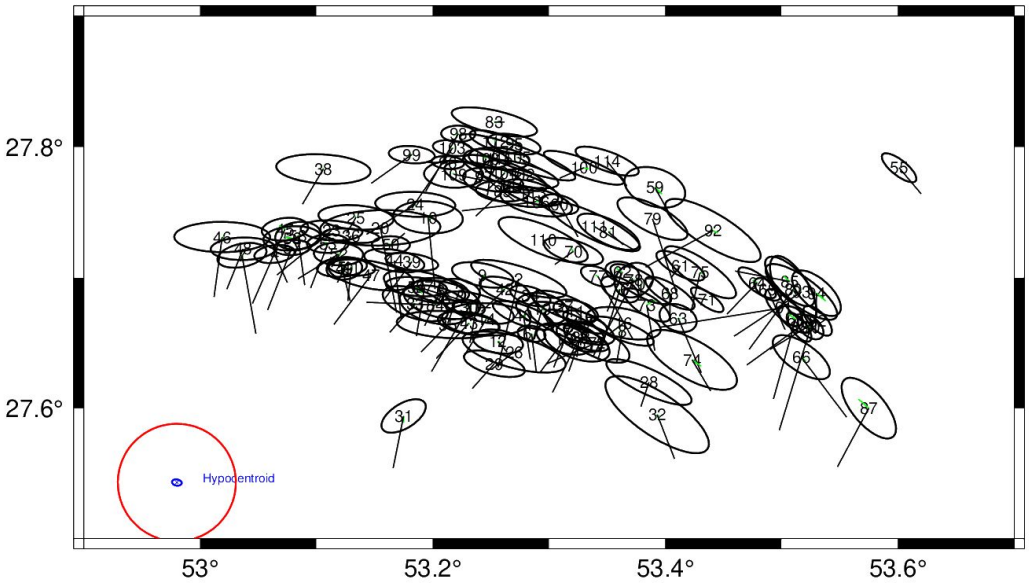

Figure S4. Relocated earthquake hypocenters with 90% confidence ellipses. The hypocentroid uncertainty is shown with the blue confidence ellipse at the bottom left corner. Numbers denote the order of events in the cluster and presented in Table S3.

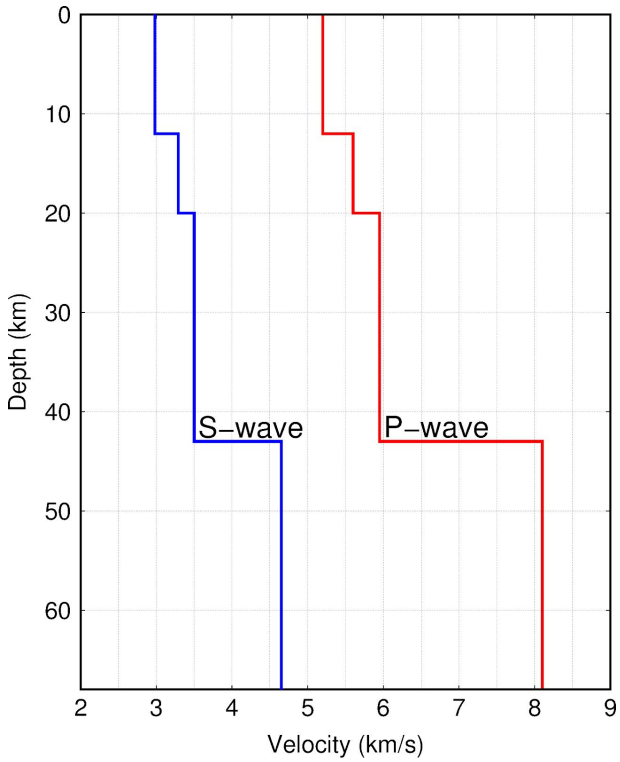

Fig S5. Regional velocity model — modified after Karasözen et al. (2019) — used for multiple-event relocation (to calculate the theoretical travel times presented in Figure S6) and calculating the Green's functions for moment tensor inversion.

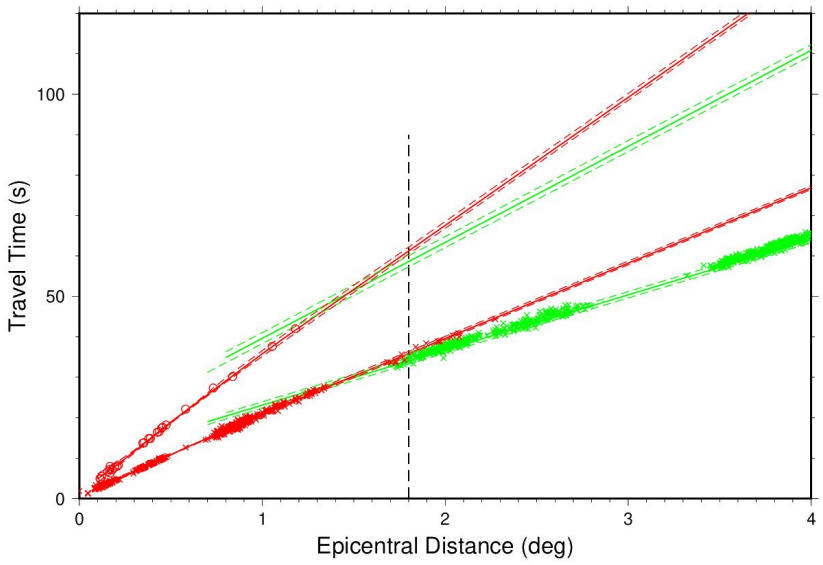

Figure S6. Fit between observed phase arrivals (Pg: Red crosses, Sg: Red circles, Pn: Green crosses) and theoretical travel times (Red and green lines) calculated from the velocity model presented in Figure S5, for epicentral distances of up to 4°.

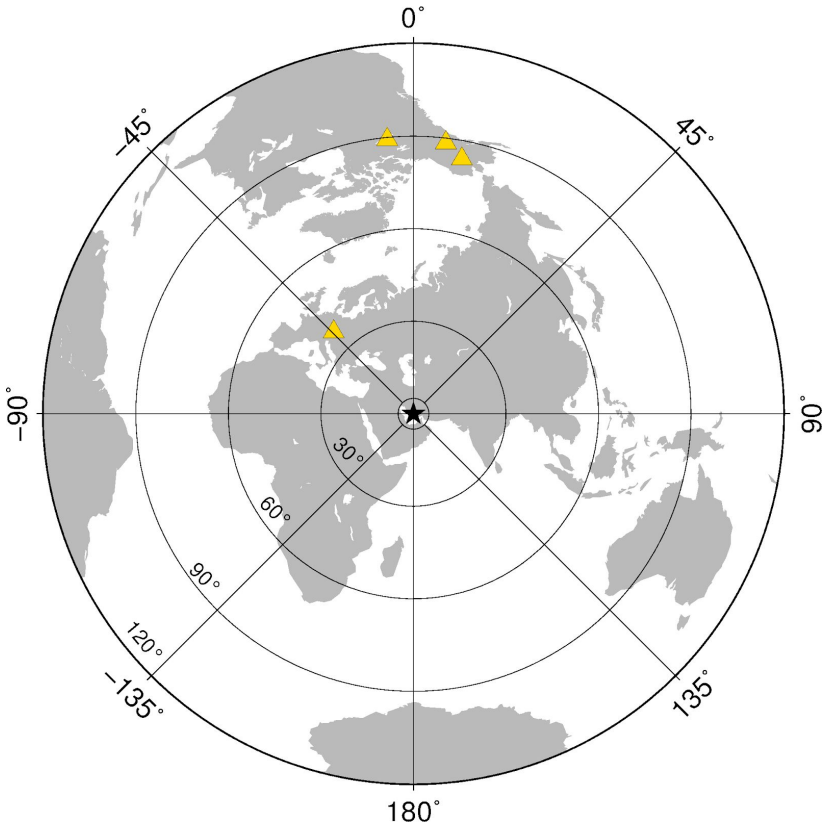

Figure S7. Yellow triangles show four different seismic arrays (BCA, IMAR, YKA, and GERES) used to improve the signal-to-noise ratio for calculation of focal depth from delay

between direct *P* and surface reflected *pP* phases. Black star shows the June 9, 2020 M_w 5.7 Khalili mainshock.

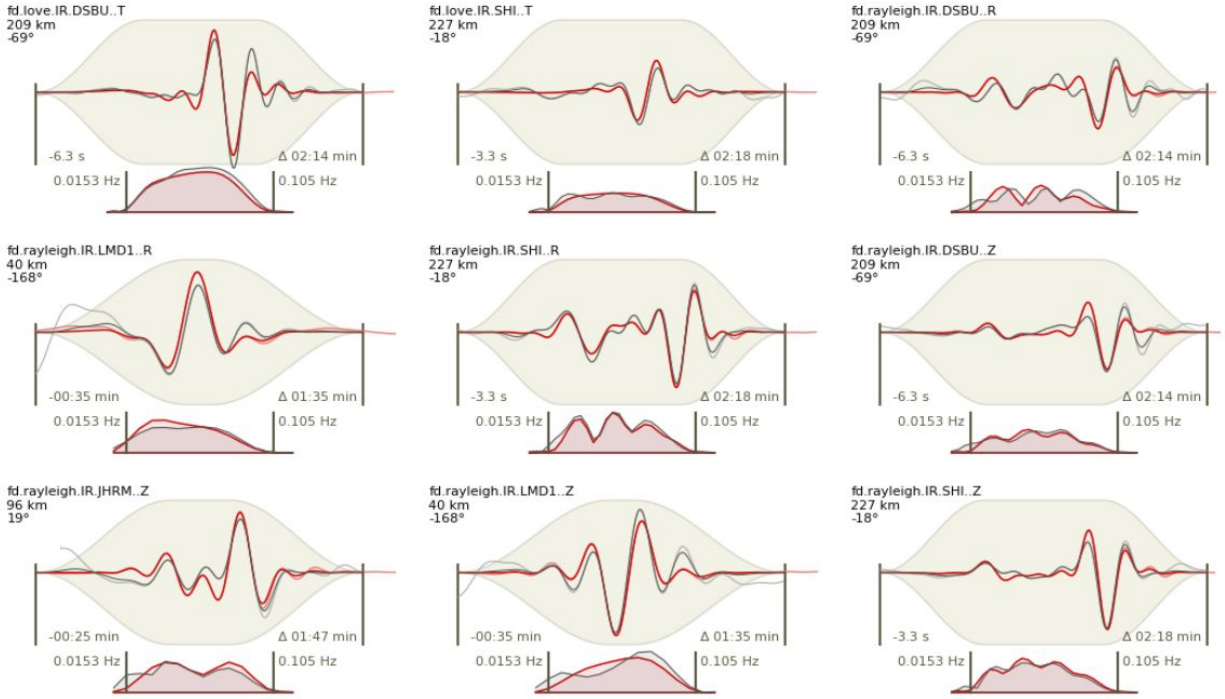

Figure S8. Waveforms fit in time domain and amplitude spectra for the June 24, 2019 M_w 4.2 normal faulting earthquake. Red and black waveforms/spectra show synthetic and observed records, respectively. Numbers within the panels describe the time window and the frequency band. Information to the left of each waveform gives (from top to bottom) the station name, component, distance to the source, and azimuth.

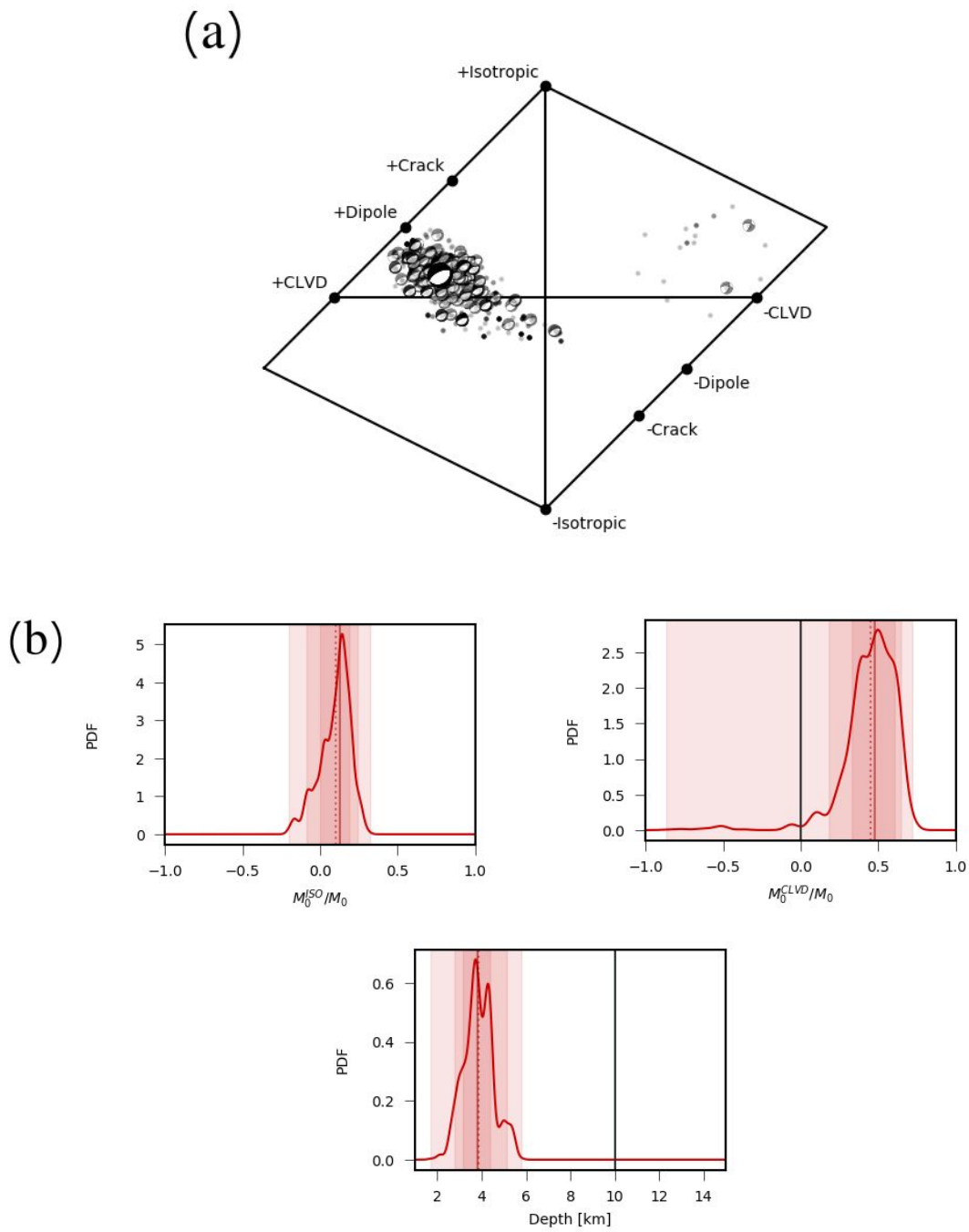

Figure S9. (a) Hudson's source type plot (Hudson, 1989) with the ensemble of bootstrap solutions, for the June 24, 2019 M_w 4.2 normal faulting earthquake. About 10% of the focal mechanisms are shown and others are represented as dots. (b) Probability density functions the CLVD, ISO and centroid depth components for the same earthquake. The plot ranges are defined by the given parameter bounds and (model space). The red solid vertical and dashed lines give the median and mean of the distribution, respectively. Dark gray vertical lines show initial values. The overlapping red-shaded areas show the 68% confidence intervals (innermost area), the 90% confidence intervals (middle area) and the minimum and maximum values (widest

area).

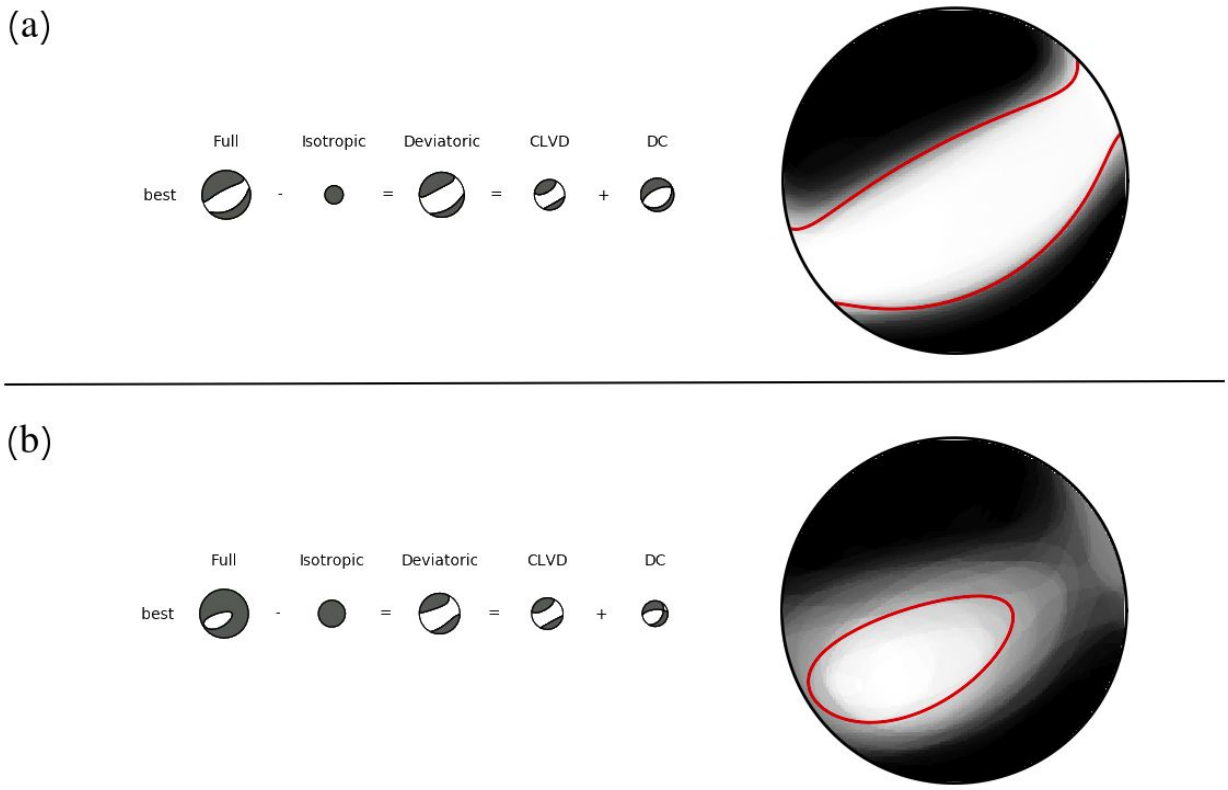

Figure S10. Moment tensor decomposition into isotropic, deviatoric and best double couple components for the two normal mechanisms in the cluster; **a)** the June 24, 2019 M_w 4.2 and **b)** The July 16, 2019 M_w 4.0. The symbol size indicates the relative strength of the components. The fuzzy moment tensors illustrate solution uncertainties. Unfortunately, no independent solution is available in the GCMT catalog or other catalogs for comparison.

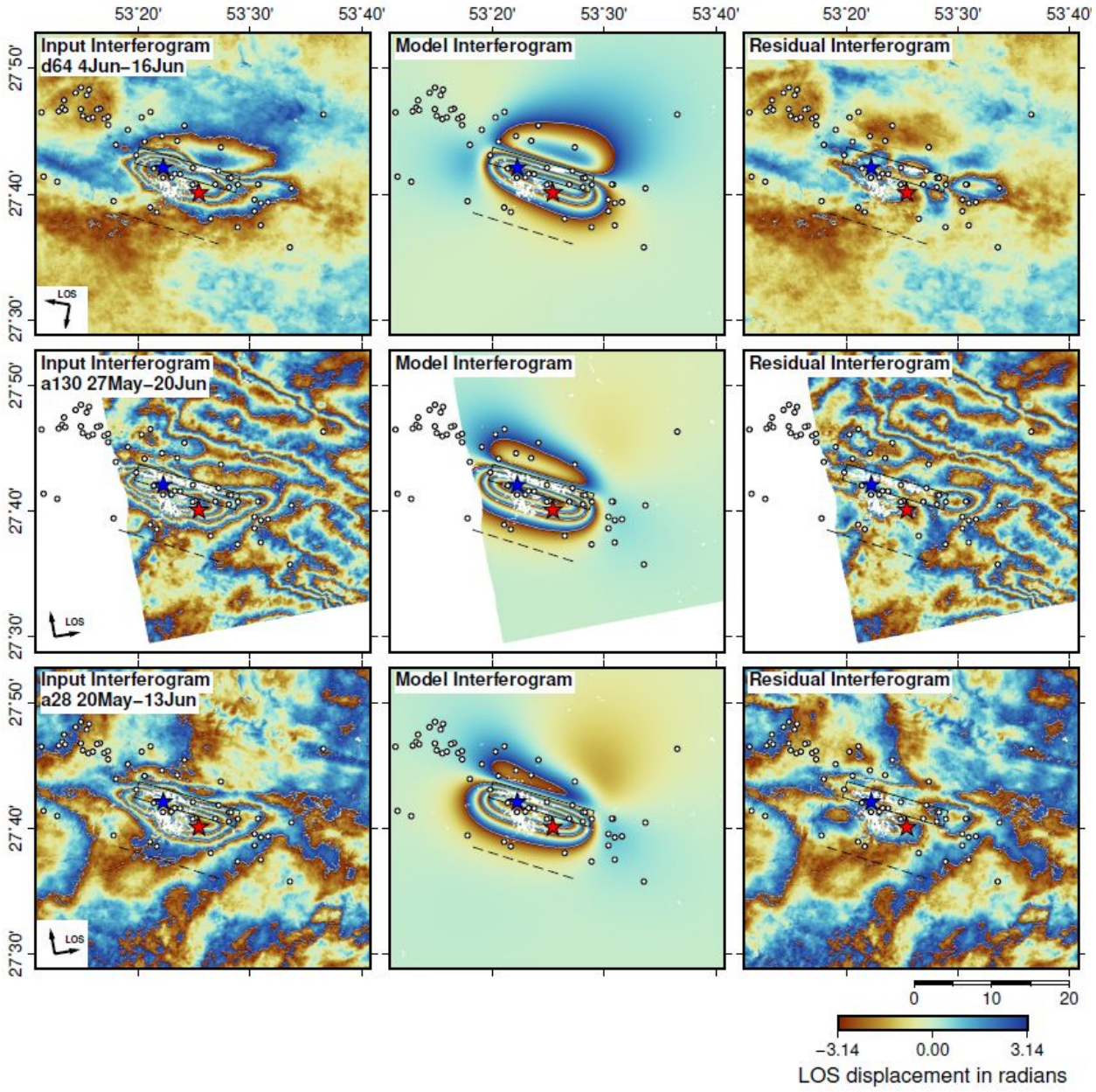

Figure S11. InSAR data (left column), model (middle) and residuals (right) for a single, NNE-dipping model fault with uniform slip (see parameters in Table S1). The three rows show Sentinel-1 tracks D64 (top), A130 (middle), and A28 (bottom). Though we inverted downsampled, unwrapped line-of-sight displacements, interferograms are shown rewrapped in order to accentuate deformation gradients. The dashed black line is the surface projection of the model fault, the black rectangle is the model fault plane outline at depth, and the red and blue stars are the relocated epicenters of the M_w 5.7 mainshock and the M_w 5.4 foreshock, respectively.

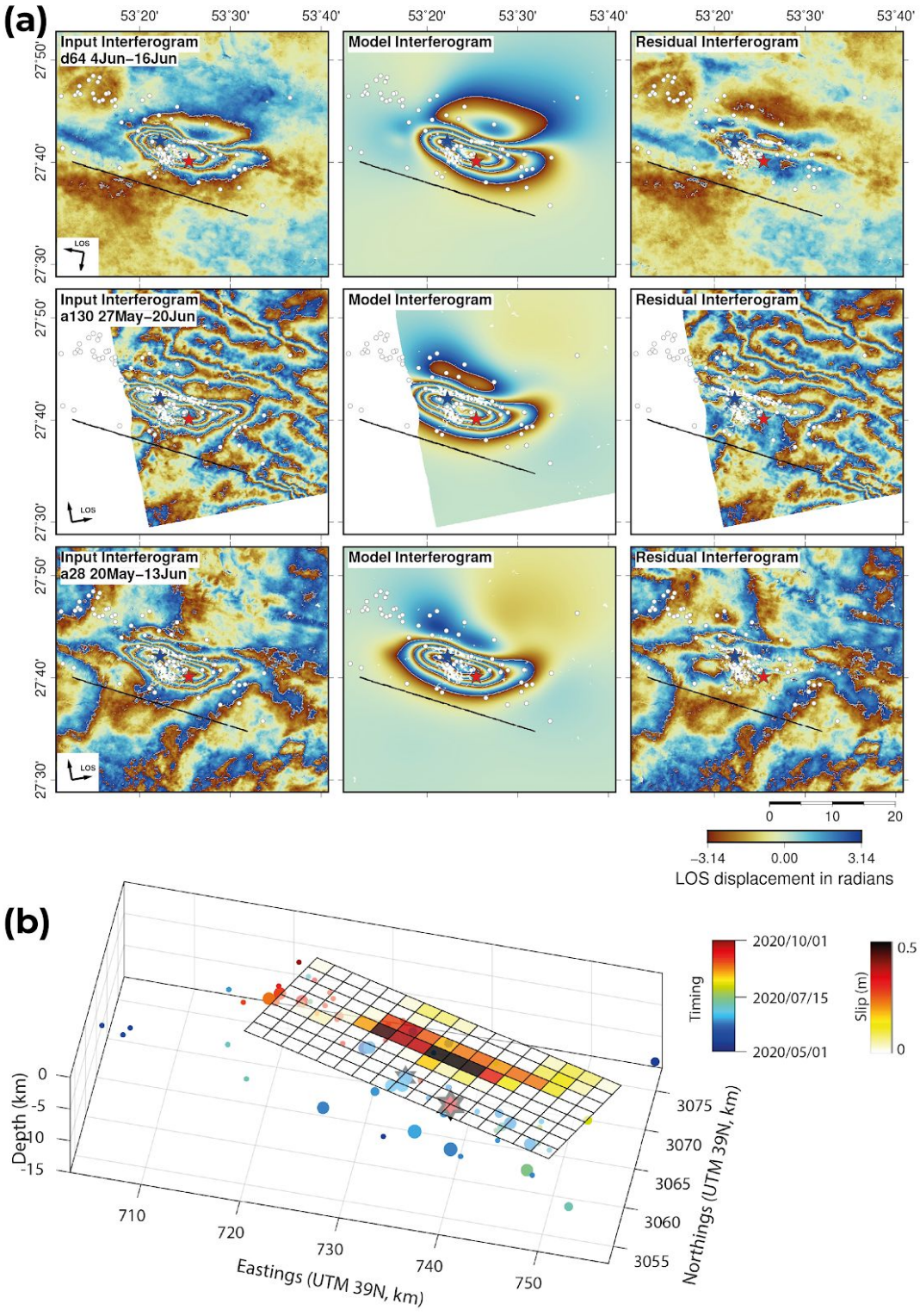

Figure S12. (a) InSAR data (left column), model (middle) and residuals (right) for a single, NNE-dipping model fault with distributed slip. The layout is otherwise the same as in Figure S11. **(b)** Model slip distribution. The model fault is divided into 2 km square patches.

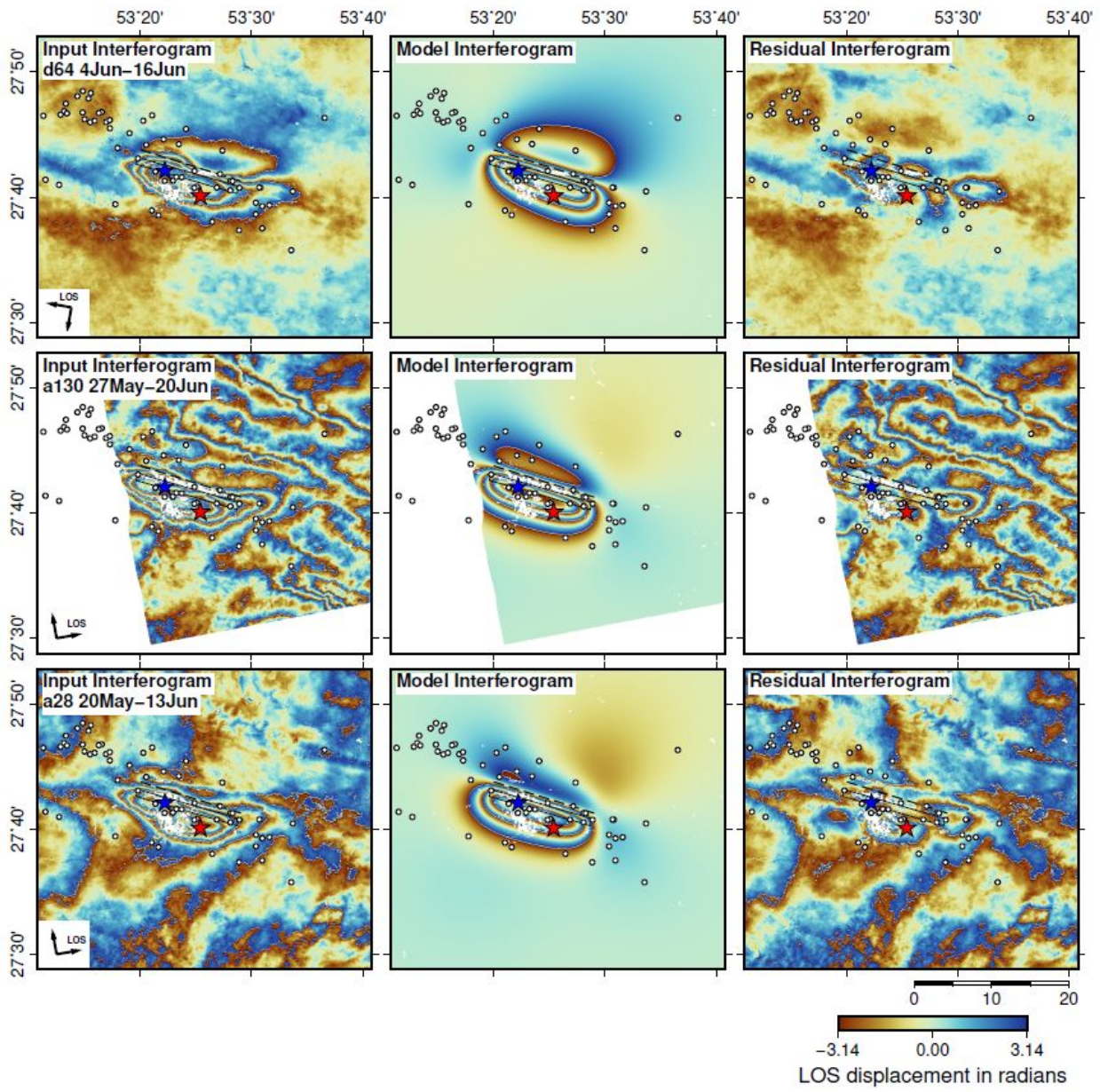

Figure S13. InSAR data (left column), model (middle) and residuals (right) for a single, SSW-dipping model fault with uniform slip (see parameters in Table S2). The layout is otherwise the same as in Figure S11.

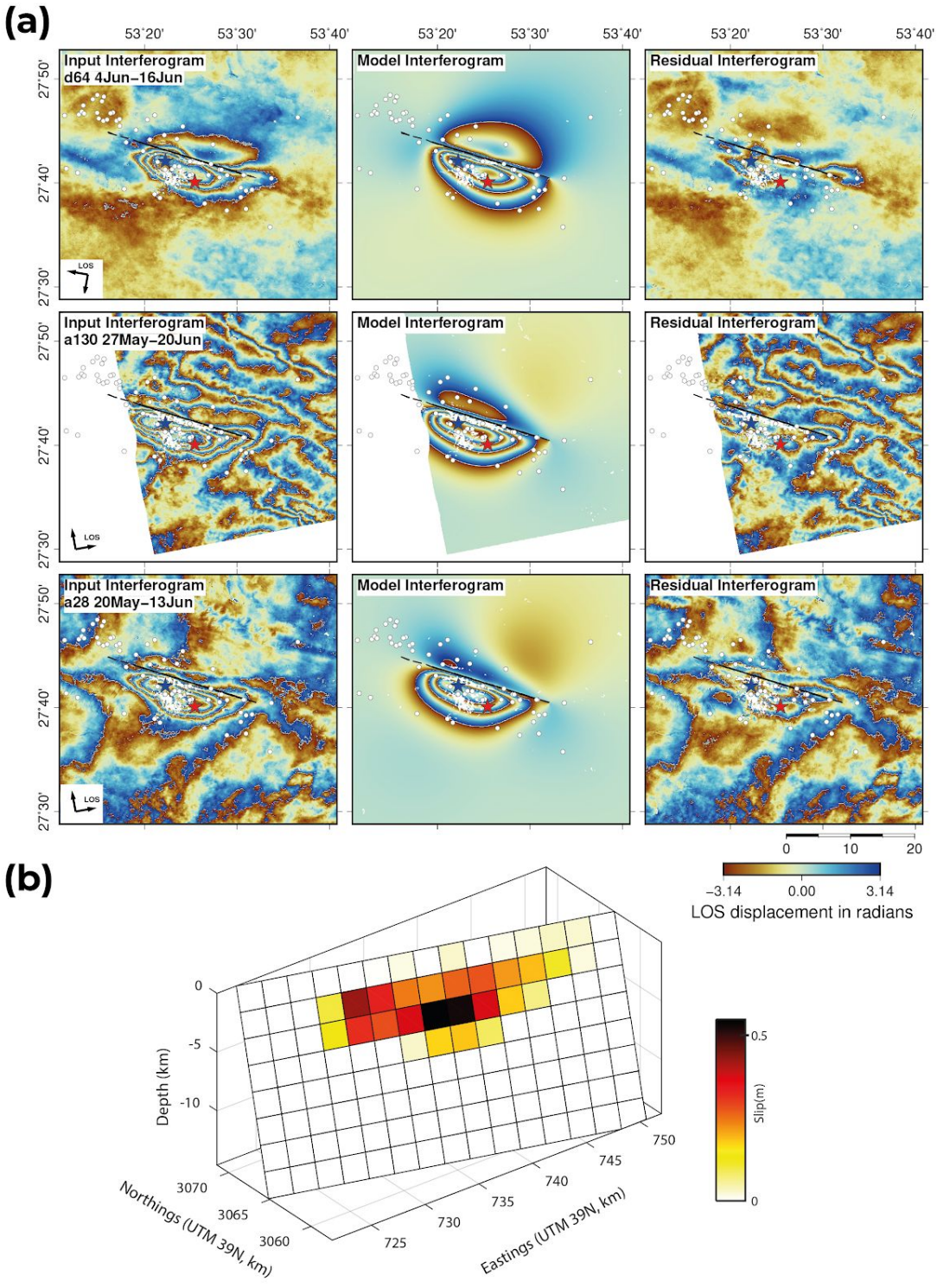

Figure S14. (a) InSAR data (left column), model (middle) and residuals (right) for a single, SSW-dipping model fault with distributed slip. **(b)** Model slip distribution. The model fault is divided into 2 km square patches.

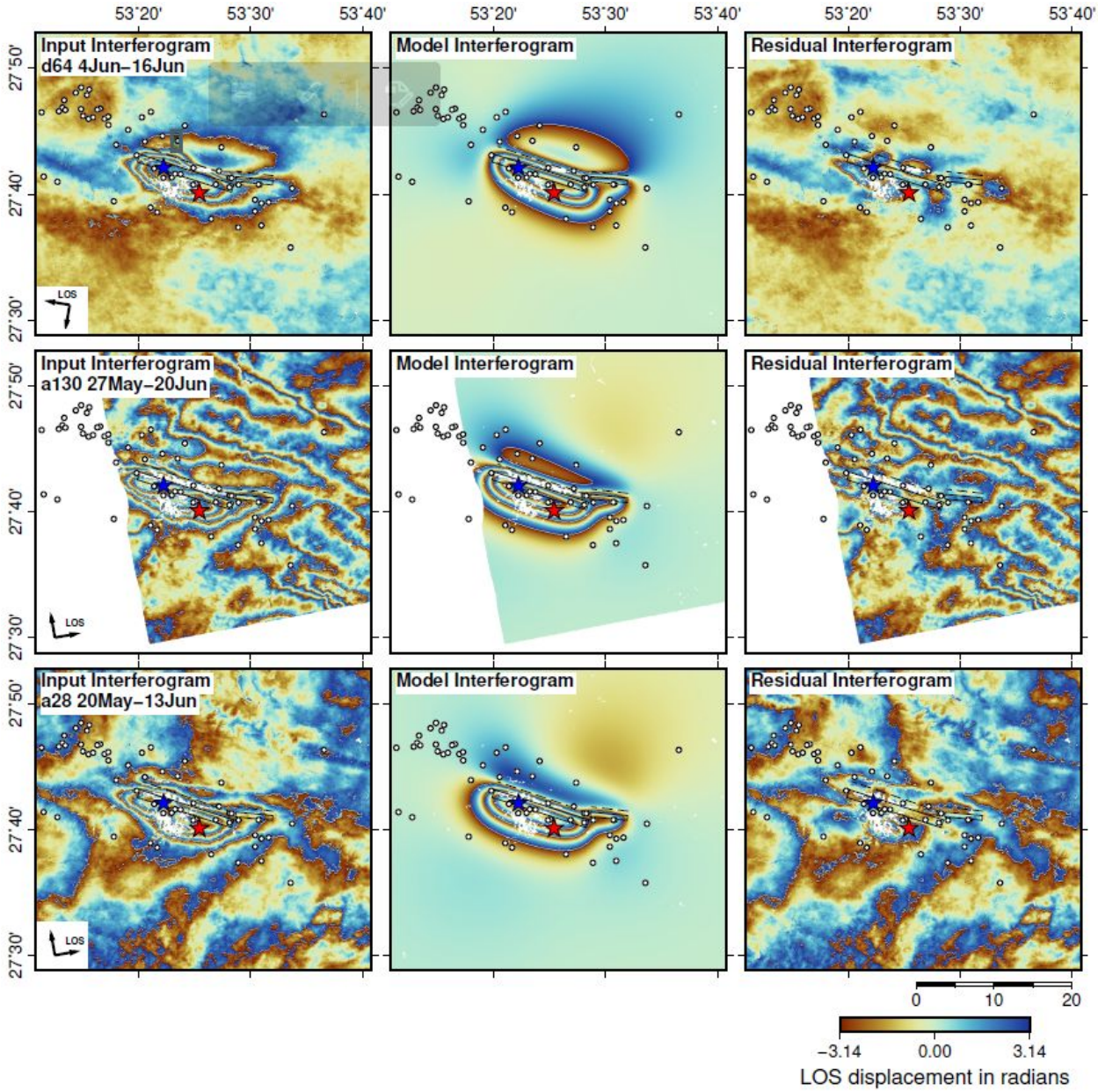

Figure S15. InSAR data (left column), model (middle) and residuals (right) for two SSW-dipping model faults with uniform slip (see parameters in Table S2). The layout is otherwise the same as in Figure S11.

	Probability (%)	Score
Q1: Has there been previous (either historical or instrumental) seismicity at the same site, or within the same regional setting?	100	1
a. Earthquakes have previously occurred in vicinity to the site, with similar rates and magnitudes: −5.		
b. Earthquakes have previously occurred within the same regional setting, with similar rates and magnitudes: −2.		
c. Earthquakes have not occurred at similar rates or magnitudes within the regional setting: +5		
d. Past earthquakes occurred at similar depths within the regional setting: −3.		
e. Earthquakes are significantly shallower than any past events that have been observed within the regional setting: +3.		
Q2: Is there temporal coincidence between the onset of events and the industrial activities?	100	5
a. The earthquake sequence began prior to the commencement of industrial activity: −15.		
b. The earthquake sequence did not begin until a significant period of time after the cessation of industrial activity: −5.		
c. The earthquake sequence began while the industrial activity was ongoing: +5.		
Q3: Are the observed seismic events temporally correlated with the injection or extraction activities?	100	4
a. The earthquakes are coincident with the industrial activity, but there is minimal correlation: −4.		
b. There is some temporal correlation between the seismicity and the industrial activity: +4.		
c. There is strong temporal correlation between the seismicity and the industrial activity (e.g., between rates of injection and rates of seismicity): +15.		
Q4: Do the events occur at similar depths to the activities?	100	3
a. Earthquakes do not occur at the same depth, and there is no plausible mechanism by which stress or pressure changes could be transferred to these depths: −4.		
b. Earthquakes do not occur at the same depth, but plausible mechanisms exist by which stress or pressure changes could be transferred to these depths: +2.		
c. Earthquakes occur at similar depths to the industrial activity: +3.		
Q5: Is there spatial collocation between events and the activities?	100	5
a. Earthquakes are distant to the activities, given the putative causative mechanism: −10.		
b. Earthquakes are sufficiently close to the activities, given the putative causative mechanism: +5.		
c. If earthquake loci change with time, this change is consistent with the industrial activity, for example, growing radially from a well or shifting in response to the start of a new well: +10.		
Q6: Is there a plausible mechanism to have caused the events?	50	1
a. No significant pore-pressure increase or decrease occurred that can be linked in a plausible manner to the event hypocentral position: −5.		
b. Some pore-pressure or poroelastic stress change occurred that can be linked in a plausible manner to the event hypocentral position: +2.		
c. A large pore-pressure or poroelastic stress change occurred that can be linked in a plausible manner to the event hypocentral position: +5.		
Q7: Do the source mechanisms indicate an induced event mechanism?	100	0
a. The source mechanisms are consistent with the regional stress conditions: 0.		
b. Source mechanisms are not consistent with the regional stress conditions, but are consistent with a putative causative mechanism (e.g., thrust faults above a subsiding reservoir): +4.		

Figure S16. Questions, answers with probability and scores for the Khalili seismic sequence according to the framework proposed by Verdon et al. (2019) for discriminating seismicity induced by industrial activities from natural earthquakes. Red text indicates the selected answer to each question. We assign a probability of 50% for question number 6 (Q6), due to lack of accurate pore pressure changes data to verify fully this question.

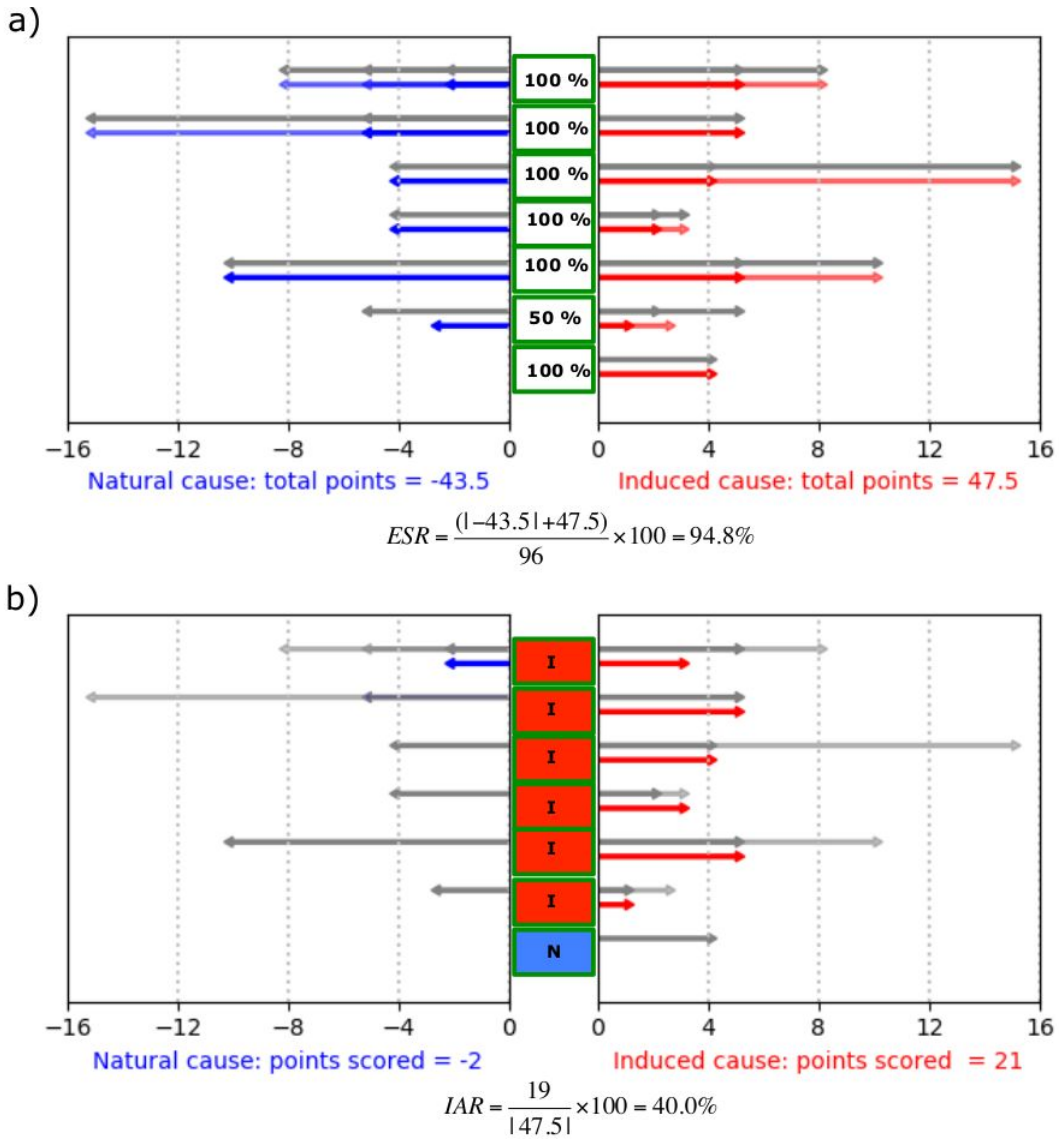

Figure S17. Schematic illustration of the evidence strength ratio (ESR) and induced assessment ratio (IAR) according to the framework proposed by Verdon et al. (2019) for discriminating the 2019-2020 Khalili seismic sequence is induced or natural. **(a)** ESR, which describes the quality and quantity of information used in the assessment. Grey arrows show the maximum points available for each question (multiple grey arrows in each question represent multiple available answers presented in Figure S16 for each question) and red and blue arrows represent the points for induced (total points = 47.5) and natural (total points = -43.5), respectively. We answer question number 6 by probability of 50%. **(b)** IAR, which categorizes the conclusion regarding the origin of the earthquake inferred from the ESR and decides whether the question and answer points to an induced (I) or natural (N). The points score of the induced and natural are -2 and 21, respectively. For the 2019-2020 Khalili seismic sequence we obtain the IAR and ESR of 40% and 95%, respectively.

Table S1: InSAR model source parameters for a single, NNE-dipping model fault with uniform slip. Eastings and Northings in km are the center of the projected surface break (UTM 39N). The strike, dip, rake, length and top and bottom depths were left as free parameters. To reduce the number of free parameters we fixed the fault slip at 0.5 meters.

Parameters	**Fault 1**
Strike (°)	286
Dip (°)	19
Rake (°)	91
Slip (m)	Fixed 0.5
Eastings (km)	737.6
Northings (km)	3067.3
Length (km)	15.4
Top depth (km)	2.7
Bottom depth (km)	3.5
Moment (Nm)	4.73×10^{17}

Table S2: InSAR model source parameters for (left) one and (right) two SSW-dipping model faults with uniform slip. Eastings and Northings in km are the center of the projected surface break (UTM 39N). The strike, dip, rake, length and top and bottom depths were left as free parameters. To reduce the number of free parameters we fixed the fault slip at 0.5 m or 0.25 m.

Parameters	**Single fault**		**Two faults**	
			West Fault	**East Fault**
Strike (°)	106		108	95
Dip (°)	66		64	66
Rake (°)	83		84	110
Slip (m)	Fixed 0.5		Fixed 0.5	Fixed 0.25
Eastings (km)	734.8		Fixed 737.5	fixed 747.0
Northings (km)	3057.5		Fixed 3067.3	Fixed 3065.8
Length (km)	15.4		14.5	5.4
Top depth (km)	2.4		2.4	1.6
Bottom depth (km)	4.8		4.8	3.2
Moment (Nm)	5.06×10^{17}		4.84×10^{17}	5.91×10^{16}

Table S3: Relocated events of the 2019-2020 Khalili seismic sequence. Date and time are given as year.month.day and hour:minute:second.millisecond format. Lat and Lon are epicentral parameters (latitude and longitude) in degrees. Depth is focal depth (km); **c** represents the fixed depth at 7 km and **n** shows the events with resolved depth by nearby station reading. The order of events (No) is the same as events number in figure S4.

No	Date	Time	Lat	Lon	Depth	Mn
1	2019.2.1	00:1:6.95	27.677	53.239	7.0c	3.3
2	2019.2.1	21:44:35.32	27.699	53.274	7.0c	3.1
3	2019.2.2	05:4:11.55	27.690	53.223	7.0c	3.5
4	2019.2.2	20:25:34.98	27.718	53.064	7.0c	3.7
5	2019.2.6	08:2:40.88	27.708	53.122	7.0c	3.4
6	2019.2.7	16:20:33.16	27.690	53.207	7.0c	3.2
7	2019.2.13	09:19:4.13	27.717	53.036	7.0c	4.0
8	2019.2.15	10:33:28.52	27.659	53.363	7.0c	3.3
9	2019.3.2	11:7:47.09	27.702	53.243	7.0c	3.4
10	2019.3.28	09:11:55.75	27.746	53.196	7.0c	3.3
11	2019.4.2	05:46:4.44	27.674	53.323	7.0c	3.3
12	2019.4.8	21:9:59.80	27.651	53.256	7.0c	3.3
13	2019.4.20	16:56:59.72	27.653	53.313	7.0c	3.4
14	2019.4.20	17:13:49.08	27.668	53.246	7.0c	3.4
15	2019.4.20	18:28:39.09	27.650	53.324	7.0c	3.2
16	2019.4.27	23:13:48.20	27.665	53.364	7.0c	3.1
17	2019.4.28	20:57:16.83	27.666	53.331	7.0c	3.3
18	2019.4.28	22:19:17.79	27.654	53.326	7.0c	3.5
19	2019.4.28	22:25:48.39	27.676	53.294	7.0c	3.5
20	2019.5.10	09:7:54.46	27.738	53.155	7.0c	3.1
21	2019.5.13	23:39:3.53	27.665	53.319	7.0c	3.1
22	2019.5.14	00:0:35.09	27.654	53.327	7.0c	3.1
23	2019.5.26	20:19:46.23	27.736	53.113	7.0c	3.1
24	2019.6.3	08:34:50.77	27.756	53.185	7.0c	3.0
25	2019.6.6	01:17:6.49	27.746	53.134	7.0c	3.3
26	2019.6.12	14:21:18.59	27.643	53.270	7.0c	3.2
27	2019.6.14	08:54:35.89	27.693	53.193	7.0c	3.3
28	2019.6.17	17:29:8.05	27.620	53.386	7.0c	3.1
29	2019.6.23	22:58:20.34	27.634	53.253	7.0c	3.2
30	2019.6.24	15:14:8.01	27.677	53.231	7.0c	4.2
31	2019.6.28	09:8:54.71	27.594	53.175	7.0c	4.2
32	2019.7.5	05:48:51.91	27.595	53.393	7.0c	3.1
33	2019.7.15	20:51:42.00	27.680	53.185	7.0c	3.2
34	2019.7.16	12:2:24.54	27.686	53.284	7.0c	4.0
35	2019.7.19	14:3:23.61	27.664	53.213	7.0c	3.3

No	Date	Time	Lat	Lon	Depth	Mn
36	2019.8.11	20:41:21.54	27.732	53.130	7.0c	3.5
37	2019.8.12	23:28:24.83	27.678	53.313	7.0c	3.0
38	2019.9.19	15:31:11.83	27.783	53.106	7.0c	3.2
39	2019.9.20	15:50:25.50	27.712	53.182	7.0c	3.5
40	2019.10.4	08:43:8.17	27.671	53.279	7.0c	3.6
41	2019.10.5	08:0:20.29	27.708	53.130	7.0c	3.6
42	2019.10.11	22:11:36.95	27.691	53.262	7.0c	3.3
43	2019.11.12	10:3:22.69	27.666	53.231	7.0c	3.2
44	2019.11.13	16:28:20.03	27.713	53.167	7.0c	3.9
45	2019.11.13	17:57:45.58	27.737	53.073	7.0c	4.2
46	2019.11.13	19:46:29.56	27.731	53.019	7.0c	3.3
47	2019.11.13	21:21:33.34	27.702	53.147	7.0c	3.4
48	2019.11.26	07:10:49.55	27.722	53.037	7.0c	3.9
49	2019.12.12	18:26:26.48	27.707	53.125	7.0c	3.1
50	2019.12.22	17:25:19.73	27.725	53.164	7.0c	3.5
51	2019.12.25	02:21:33.34	27.663	53.322	5 n	3.1
52	2020.2.13	13:41:40.27	27.718	53.119	7.0c	3.3
53	2020.2.14	04:11:34.35	27.726	53.110	7.0c	3.5
54	2020.3.21	19:25:23.73	27.693	53.186	10 n	3.1
55	2020.5.12	13:50:51.07	27.784	53.601	7.0c	3.7
56	2020.5.16	18:17:35.55	27.730	53.079	7.0c	3.1
57	2020.5.16	18:20:22.52	27.723	53.079	7.0c	3.4
58	2020.5.16	022:41:8.98	27.732	53.084	7.0c	3.1
59	2020.5.30	22:55:29.39	27.769	53.391	7.0c	3.6
60	2020.5.31	23:59:0.95	27.756	53.309	10 n	4.7
61	2020.6.1	07:41:34.12	27.709	53.413	7.0c	3.3
62	2020.6.9	16:8:48.78	27.704	53.363	7 n	5.4
63	2020.6.9	17:18:12.47	27.669	53.411	7 n	5.7
64	2020.6.9	17:43:17.27	27.696	53.479	7.0c	3.7
65	2020.6.9	19:44:53.53	27.668	53.512	7.0c	4.0
66	2020.6.9	21:55:10.55	27.639	53.517	7.0c	3.3
67	2020.6.9	22:26:58.96	27.657	53.285	9 n	4.1
68	2020.6.9	23:9:38.39	27.688	53.404	4 n	3.0
69	2020.6.10	04:2:26.66	27.691	53.488	7.0c	4.1
70	2020.6.10	5:52:11.26	27.720	53.321	6 n	4.0
71	2020.6.11	2:41:54.88	27.683	53.436	8 n	3.3
72	2020.6.12	3:34:49.82	27.650	53.341	3 n	3.6
73	2020.6.12	04:4:56.48	27.679	53.384	11 n	3.8
74	2020.6.12	13:49:38.88	27.637	53.423	7.0c	3.0
75	2020.6.12	21:34:3.16	27.704	53.430	7.0c	3.1
76	2020.6.13	22:4:14.29	27.691	53.361	7 n	4.8
77	2020.6.13	23:15:3.40	27.701	53.342	10 n	4.6
78	2020.6.14	18:6:0.06	27.698	53.373	14 n	5.2
79	2020.6.15	09:7:49.05	27.745	53.389	7.0c	3.3
80	2020.6.19	06:8:0.15	27.691	53.510	7.0c	3.3
81	2020.6.21	08:5:40.99	27.735	53.351	7.0c	3.8
82	2020.6.23	09:29:58.86	27.667	53.531	7.0c	3.3

No	Date	Time	Lat	Lon	Depth	Mn
83	2020.6.28	23:5:32.02	27.819	53.253	7.0c	3.2
84	2020.7.1	08:45:38.38	27.679	53.202	7.0c	3.3
85	2020.7.3	3:46:41.45	27.697	53.507	7.0c	3.5
86	2020.7.4	9:1:56.79	27.683	53.208	9 n	3.0
87	2020.7.4	09:4:27.09	27.600	53.575	7.0c	3.6
88	2020.7.7	17:40:41.34	27.662	53.515	7.0c	3.3
89	2020.7.10	15:41:37.41	27.766	53.260	7.0c	3.2
90	2020.7.10	20:14:4.57	27.662	53.525	7.0c	4.5
91	2020.7.10	20:22:3.77	27.677	53.502	7.0c	3.1
92	2020.7.13	02:2:34.49	27.736	53.441	7.0c	3.1
93	2020.7.20	14:36:56.20	27.689	53.517	7.0c	3.1
94	2020.7.28	23:10:22.59	27.688	53.530	7.0c	3.6
95	2020.8.21	05:16:3.56	27.802	53.270	7.0c	3.7
96	2020.8.25	12:16:0.10	27.788	53.213	7.0c	4.2
97	2020.8.25	12:25:16.21	27.777	53.244	7.0c	3.4
98	2020.8.31	03:36:50.50	27.810	53.222	7.0c	4.8
99	2020.8.31	05:28:25.13	27.794	53.182	7.0c	3.4
100	2020.8.31	06:1:50.06	27.784	53.330	7.0c	3.2
101	2020.8.31	07:47:6.43	27.769	53.267	7.0c	3.1
102	2020.8.31	10:40:33.14	27.779	53.276	7.0c	3.3
103	2020.8.31	15:57:19.77	27.799	53.217	7.0c	3.7
104	2020.8.31	17:57:49.91	27.780	53.262	7.0c	3.2
105	2020.8.31	21:12:43.35	27.792	53.273	7.0c	3.0
106	2020.9.3	17:30:9.50	27.758	53.289	7.0c	3.2
107	2020.9.4	02:23:50.08	27.695	53.379	7 n	3.1
108	2020.9.8	01:34:17.49	27.791	53.246	7.0c	4.3
109	2020.9.8	02:38:21.55	27.779	53.218	7.0c	3.1
110	2020.9.8	06:5:31.37	27.729	53.295	9 n	3.2
111	2020.9.9	11:27:57.25	27.739	53.339	8 n	3.1
112	2020.9.10	05:10:17.54	27.805	53.254	7.0c	3.2
113	2020.9.19	17:1:33.05	27.765	53.286	10 n	3.5
114	2020.9.21	09:22:12.64	27.789	53.350	7.0c	3.3
115	2020.9.28	03:30:24.22	27.791	53.257	7.0c	3.3

References

Elliott, J. R., Bergman, E. A., Copley, A. C., Ghods, A. R., Nissen, E. K., Oveisi, B., et al. (2015). The 2013 Mw 6.2 Khaki-Shonbe (Iran) Earthquake: Insights into seismic and aseismic shortening of the Zagros sedimentary cover. *Earth and Space Science*, *2*(11), 435–471. https://doi.org/10.1002/2015EA000098

Funning, G. J., Parsons, B., Wright, T. J., Jackson, J. A., & Fielding, E. J. (2005). Surface displacements and source parameters of the 2003 Bam (Iran) earthquake from Envisat advanced synthetic aperture radar imagery. *Journal of Geophysical Research: Solid Earth*, *110*(B9). https://doi.org/10.1029/2004JB003338

Hudson, J. A., Pearce, R. G., & Rogers, R. M. (1989). Source type plot for inversion of the moment tensor. *Journal of Geophysical Research: Solid Earth*, *94*(B1), 765–774. https://doi.org/10.1029/JB094iB01p00765

Jonsson, S., Zebker H., Segall P., Amelung F. (2002). Fault slip distribution of the Mw 7.2 Hector Mine earthquake estimated from satellite radar and GPS measurements. *Bulletin of the Seismological Society of America*. 92, 1377–1389. https://doi.org/10.1785/0120000922.

Karasözen, E., Nissen, E., Bergman, E. A., & Ghods, A. (2019). Seismotectonics of the Zagros (Iran) From Orogen-Wide, Calibrated Earthquake Relocations. *Journal of Geophysical Research: Solid Earth*, *124*(8), 9109–9129. https://doi.org/10.1029/2019JB017336

Nissen, E., Yamini-Fard, F., Tatar, M., Gholamzadeh, A., Bergman, E., Elliott, J. R., et al. (2010). The vertical separation of mainshock rupture and microseismicity at Qeshm island in the Zagros fold-and-thrust belt, Iran. *Earth and Planetary Science Letters*, *296*(3), 181–194. https://doi.org/10.1016/j.epsl.2010.04.049

Okada, Y. (1985). Surface deformation due to shear and tensile faults in a half-space. *Bulletin of the Seismological Society of America*, *75*(4), 1135–1154.

Verdon, J. P., Baptie, B. J., & Bommer, J. J. (2019). An Improved Framework for Discriminating Seismicity Induced by Industrial Activities from Natural EarthquakesAn Improved Framework for Discriminating Seismicity Induced by Industrial Activities from Natural Earthquakes. *Seismological Research Letters*, *90*(4), 1592–1611. https://doi.org/10.1785/0220190030

Wright, T. J., Parsons, B. E., Jackson, J. A., Haynes, M., Fielding, E. J., England, P. C., & Clarke, P. J. (1999). Source parameters of the 1 October 1995 Dinar (Turkey) earthquake from SAR interferometry and seismic bodywave modelling. *Earth and Planetary Science Letters*, *172*(1), 23–37. https://doi.org/10.1016/S0012-821X(99)00186-7